International Journal for Numerical Methods in Fluids

WILEY

RESEARCH ARTICLE OPEN ACCESS

Polymer Stress-Tensor Calculation for a Laminar Submerged Viscoelastic Jet Flow Using Different Constitutive Models

Rafael de Lima Sterza[1] | Leandro Franco de Souza[1] | Marcio Teixeira de Mendonca[2] | Analice Costacurta Brandi[3]

[1]Department of Applied Mathematics and Statistics, University of São Paulo, São Paulo, Brazil | [2]National Institute of Space Research, INPE, São Paulo, Brazil | [3]Department of Mathematics and Computer Science, São Paulo State University, São Paulo, Brazil

Correspondence: Leandro Franco de Souza (lefraso@icmc.usp.br)

Received: 3 July 2025 | **Revised:** 25 November 2025 | **Accepted:** 5 January 2026

Keywords: planar jet flow | polymer stress tensor | viscoelastic models

ABSTRACT

Viscoelastic fluids, exhibiting both elastic and viscous properties, play a fundamental role in various industrial and biological applications. Accurate modeling of their rheological behavior requires constitutive equations that capture the complex interplay between these properties. The present study focuses on the analysis of incompressible, isothermal, two-dimensional, planar, laminar, submerged jet flow of viscoelastic fluids. A computational methodology is adopted to determine the polymer stress-tensor distribution for different viscoelastic models, including Oldroyd-B, UCM, Giesekus, Phan-Thien-Tanner (PTT), and finitely extensible nonlinear elastic (FENE). These models are chosen to represent a diverse range of viscoelastic behaviors. The Navier–Stokes equations, coupled with the appropriate constitutive model, are solved numerically. The proposed method allows one to access the distribution of the polymer stress-tensor components with very low computational cost. Results demonstrate the accuracy of the computational method for various models and their parameter values. The findings provide valuable insights into the fundamental behavior of viscoelastic jets and can serve as a foundation for subsequent linear and nonlinear stability investigations.

1 | Introduction

Viscoelastic fluids are being used more frequently in industrial and biologic settings for many purposes, including some electronic appliances and DNA technologies [1]. These fluids are complex and have both elastic and viscous characteristics, making it difficult to comprehend how they behave. Several constitutive equations are used to try to describe the rheological behavior of polymeric fluids. These equations can be divided into several categories based on their structure, mathematical composition, and capacity to predict material functions. Numerous articles in the literature address constitutive models of viscoelastic fluids, including the Maxwell differentials [2, 3], Oldroyd-B [3–6], Giesekus [7], Leonov [8], finitely extensible nonlinear elastic (FENE) [9, 10], Phan-Thien-Tanner (PTT) [6, 11]. Additionally, models derived from the Pom theory [12] are also explored. Integral models, such as Maxwell [13] and K-BKZ [14, 15], are also frequently discussed. A key component in describing flow patterns is the flow variables distribution, which is the solution of the Navier-Stokes equations, used as a benchmark for the examination of more intricate phenomena, like phase transitions and hydrodynamic instabilities.

Although the Oldroyd-B model offers a means of deriving flow solutions between flat plates, the process depends on specific assumptions. Therefore, obtaining such solutions remains

https://doi.org/10.1002/fld.70058

challenging across various existing models. Researchers have extensively investigated solutions to the Navier-Stokes equations for viscoelastic fluids, such as Couette and Poiseuille flows. Yoo and Choi [16] and Schleiniger and Weinacht [17] provided solutions for the Giesekus model pipe and channel flows related to Poiseuille flow. Oliveira [18] found an exact solution for tube and slit flows of a FENE-P fluid. The Oldroyd-B model exact solution applied to five different flow problems was found by Hayat et al. [19] and then Hayat et al. [20] expanded this to six different unsteady flow problems. Raisi et al. [21] found the Couette-Poiseuille flow solution using the same model. Based on Schleiniger and Weinacht [17], Tomé et al. [22] presented a method to derive an analytical solution for the Giesekus model, taking into account that the fluid is entirely polymeric, and involves numerically computing pressure gradients. An analytical solution for the Giesekus model parameters was studied by Furlan et al. [23] and, recently, Araujo et al. [24] used the linear Phan-Thien-Tanner (LPTT) constitutive equation to present a semi-analytical method for laminar steady-state channel and pipe flows of viscoelastic fluids, taking solvent viscosity contributions into account.

However, in the case of viscoelastic jet flows, analytical solutions are particularly challenging to obtain due to the imposed conditions and complex fluid behavior. For instance, for a laminar two-dimensional jet, assuming the ambient fluid to be of the same fluid as the jet itself, some of this ambient fluid is carried along with the jet by the viscous drag at the outer edge of the jet, Schlichting [25] and Kundu et al. [26] present, via a differential equation for the stream function, the velocity distribution for jet flow in a Newtonian fluid. Michalke [27] proposes the discussion of four velocity profiles that are relevant to study the stability of the flow field in a circular free jet. These velocity distributions are also used in other works [28–31]. In the case of flows for non-Newtonian fluids, Parvar et al. [32] presents a local self-similar solution for the laminar planar jet flow of viscoelastic fluids, described by the FENE-P constitutive equation, through an order of magnitude simplification of the governing equations. According to Guimarães et al. [33], Guimarães carried out the first direct numerical simulation (DNS) of turbulent viscoelastic jets. Developing a theory to describe turbulent planar jets of viscoelastic fluids, based on the classical thin shear-layer approximation, they performed a DNS of spatially evolving turbulent planar jets of viscoelastic fluids described by the FENE-P model [33–37]. Yamani et al. [38] conducted an experimental study on elastoinertial turbulence (EIT) in planar viscoelastic jets. Their results demonstrate that fluid elasticity plays a key role in the transition to turbulence, inducing instabilities in both the shear layer and the jet column.

In this context, this article aims to obtain the polymer stress-tensor components of a viscoelastic jet flow, focusing on incompressible, isothermal, two-dimensional, planar, laminar, submerged jets discharging into a medium of the same fluid, using Oldroyd-B, UCM (Upper-Convected-Maxwell), Giesekus, PTT, and FENE models for the constitutive equation. The study presents results for the computation of the polymer stress components for different non-Newtonian parameters and constitutive models, given a fixed velocity profile and considering a stationary and parallel flow to simplify the equations. Imposing a fixed velocity profile is frequently used in local hydrodynamic stability analysis, where the stability of the flow is determined for a given frozen base flow. For non-Newtonian flow problems, given a local base flow velocity distribution, the stability analysis also requires the corresponding base flow stress-tensor components. The presented method provides a more cost-effective alternative for evaluating polymer stress tensors compared to solving the complete equations. Moreover, this approach is suitable for flows with slow variation in the streamwise direction, even when it is not feasible to reduce the equations to a parabolic form using a boundary-layer-like approximation.

The paper is organized as follows. Section 2 presents the governing equations and mathematical manipulations; the numerical method used is presented in Section 3. The results obtained using the method proposed are presented in Section 4. The main conclusions are presented in Section 5.

2 | Mathematical Formulation

The flow under consideration is governed by the mass and momentum equations, which are expressed as follows, assuming a incompressible, isothermal, and non-Newtonian (viscoelastic) behavior:

$$\nabla \cdot \mathbf{u} = 0, \tag{1}$$

$$\frac{\partial \mathbf{u}}{\partial t} + \nabla \cdot (\mathbf{u}\mathbf{u}) = -\nabla p + \frac{\beta_n}{Re}\nabla^2 \mathbf{u} + \nabla \cdot \mathbf{T}, \tag{2}$$

where $\mathbf{u}$ denotes the velocity field, t is the time, p is the pressure, $\beta_n = \eta_s/\eta_0$ is the dimensionless coefficient of the solvent viscosity (where $\eta_0 = \eta_s + \eta_p$, with η_0 being the total viscosity, η_s and η_p being the solvent and polymer viscosity, respectively), $Re = (\rho U_s L_s)/\eta_0$ is the Reynolds number, ρ is the fluid density, L_s is the length scale (for the jet flow it is the jet half-width), U_s is the velocity scale and $\mathbf{T}$ is the polymer stress tensor. The tensors are modeled by constitutive equations that allow the study of viscoelastic fluids. The viscoelastic fluid model employed in this analysis is characterized by its dimensionless form, which is expressed as follows:

$$\begin{aligned} f(tr(\mathbf{T}))\mathbf{T} + Wi\left[\frac{\partial \mathbf{T}}{\partial t} + \nabla \cdot (\mathbf{u}\mathbf{T}) - \nabla \mathbf{u} \cdot \mathbf{T} - \mathbf{T} \cdot \nabla \mathbf{u}^T\right] \\ + \xi Wi\left(\mathbf{D} \cdot \mathbf{T} + \mathbf{T} \cdot \mathbf{D}^T\right) + \frac{\alpha_G Re Wi}{(1-\beta_n)}(\mathbf{T} \cdot \mathbf{T}) = 2\frac{(1-\beta_n)}{Re}\mathbf{D}, \end{aligned} \tag{3}$$

where $\mathbf{D}$ is the deformation-rate tensor, $Wi = \lambda U_s/L_s$ denotes the Weissenberg number, λ is the relaxation-time of the fluid, α_G is the so-called mobility parameter, if $\alpha_G = 0$ the constitutive equation corresponds to the Oldroyd-B model. Although the theoretical range of the mobility parameter is $0 < \alpha_G < 1$, physically realistic solutions are only obtained for $0 < \alpha_G < 0.5$ [39]. The term $f(tr(\mathbf{T}))$ represents the trace function of the tensor $\mathbf{T}$ which determines the form of the PTT model [11, 40]:

- Linear (LPTT): $f(tr(\mathbf{T})) = 1 + \varepsilon \frac{ReWi}{(1-\beta_n)} tr(\mathbf{T})$,
- Quadratic (QPTT): $f(tr(\mathbf{T})) = 1 + \varepsilon \frac{ReWi}{(1-\beta_n)} tr(\mathbf{T}) + \frac{1}{2}\varepsilon \left[\frac{ReWi}{(1-\beta_n)} tr(\mathbf{T})\right]^2$,

- Exponential (EPTT): $f(tr(\mathbf{T})) = \exp\left[\varepsilon \frac{ReWi}{(1-\beta_n)} tr(\mathbf{T})\right]$,

where $tr(\mathbf{T})$ is the trace of the polymer stress tensor $\mathbf{T}$. The parameter ξ is positive and is related to differences in normal stress components. The parameter ε is associated with the elongational behavior of the fluid, preventing the possibility of an infinite elongational viscosity in a simple stretching flow, which would occur in models such as Maxwell's (UCM or Oldroyd-B) [41].

The constitutive equation employed for the viscoelastic tensors in the FENE models will be expressed in terms of the tensor conformation $\mathbf{A}$ provided by:

$$\frac{\partial \mathbf{A}}{\partial t} + \nabla \cdot (\mathbf{uA}) - \nabla \mathbf{u} \cdot \mathbf{A} - \mathbf{A} \cdot \nabla \mathbf{u}^T = \frac{1}{Wi} P(\mathbf{A}), \tag{4}$$

where $P(\mathbf{A})$ is a tensor that depends on $\mathbf{A}$ as established by the constitutive model. Furthermore, through the conformation tensor $\mathbf{A}$, it is possible to obtain the polymer stress tensor:

- Oldroyd-B:

$$P(\mathbf{A}) = \mathbf{I} - \mathbf{A}, \qquad \mathbf{T} = \kappa(\mathbf{A} - \mathbf{I}). \tag{5}$$

- Giesekus:

$$P(\mathbf{A}) = (\mathbf{I} - \mathbf{A})[\mathbf{I} + \alpha_G(\mathbf{A} - \mathbf{I})], \qquad \mathbf{T} = \kappa(\mathbf{A} - \mathbf{I}). \tag{6}$$

- FENE-P:

$$\begin{aligned} f(\mathbf{A}) &= \frac{L^2}{L^2 - tr(\mathbf{A})}, \quad P(\mathbf{A}) = f(L)\mathbf{I} - f(\mathbf{A})\mathbf{A}, \\ \mathbf{T} &= \kappa[f(\mathbf{A})\mathbf{A} - f(L)\mathbf{I}]. \end{aligned} \tag{7}$$

- FENE-CR:

$$\begin{aligned} f(\mathbf{A}) &= \frac{L^2}{L^2 - tr(\mathbf{A})}, \qquad P(\mathbf{A}) = f(\mathbf{A})[\mathbf{I} - \mathbf{A}], \\ \mathbf{T} &= \kappa f(\mathbf{A})(\mathbf{A} - \mathbf{I}), \end{aligned} \tag{8}$$

where $\kappa = \dfrac{1-\beta_n}{ReWi}$, L is the maximum extension of the polymer, $tr(\mathbf{A})$ is the trace of the conformation tensor and $f(L) = \dfrac{L^2}{L^2-3}$, the functions $f(\mathbf{A})$ and $f(L)$ depend on the chosen Peterlin function for FENE-P model Parvar et al. [32]. Note that the conformation-tensor formulation also allows for obtaining the Oldroyd-B and Giesekus models. Furthermore, as $L \to \infty$ in the FENE models, it leads to the Oldroyd-B model and $f(\mathbf{A}) = f(L) = 1$ for Oldroyd-B and Giesekus models.

In this study, both formulations will be used to determine the components of the polymer stress tensors. However, when applying the conformation-tensor formulation, the relations in Equations (5–8) will be employed to compute $\mathbf{T}$ from $\mathbf{A}$, as all comparisons will be made using the polymer stress tensor.

Thus, we can express Equations (1–4) in two-dimensional Cartesian coordinates as follows:

$$\frac{\partial u}{\partial x} + \frac{\partial v}{\partial y} = 0, \tag{9}$$

$$\begin{aligned} &\frac{\partial u}{\partial t} + \frac{\partial (uu)}{\partial x} + \frac{\partial (uv)}{\partial y} = -\frac{\partial p}{\partial x} + \frac{\beta_n}{Re}\left[\frac{\partial^2 u}{\partial x^2} + \frac{\partial^2 u}{\partial y^2}\right] \\ &\quad + \frac{\partial T_{xx}}{\partial x} + \frac{\partial T_{xy}}{\partial y}, \frac{\partial v}{\partial t} + \frac{\partial (uv)}{\partial x} + \frac{\partial (vv)}{\partial y} \\ &\quad = -\frac{\partial p}{\partial y} + \frac{\beta_n}{Re}\left[\frac{\partial^2 v}{\partial x^2} + \frac{\partial^2 v}{\partial y^2}\right] + \frac{\partial T_{xy}}{\partial x} + \frac{\partial T_{yy}}{\partial y}, \end{aligned} \tag{10}$$

$$\begin{aligned} &f(tr(\mathbf{T}))T_{xx} + Wi\left(\frac{\partial T_{xx}}{\partial t} + \frac{\partial (uT_{xx})}{\partial x} + \frac{\partial (vT_{xx})}{\partial y}\right. \\ &\quad \left. -2T_{xx}\frac{\partial u}{\partial x} - 2T_{xy}\frac{\partial u}{\partial y} + +\xi\left[2T_{xx}\frac{\partial u}{\partial x} + T_{xy}\left(\frac{\partial u}{\partial y} + \frac{\partial v}{\partial x}\right)\right]\right) \\ &\quad + \frac{\alpha_G ReWi}{(1-\beta_n)}\left(T_{xx}^2 + T_{xy}^2\right) = 2\frac{(1-\beta_n)}{Re}\frac{\partial u}{\partial x}, \end{aligned} \tag{11}$$

$$\begin{aligned} &f(tr(\mathbf{T}))T_{yy} + Wi\left(\frac{\partial T_{yy}}{\partial t} + \frac{\partial (uT_{yy})}{\partial x} + \frac{\partial (vT_{yy})}{\partial y}\right. \\ &\quad \left. -2T_{xy}\frac{\partial v}{\partial x} - 2T_{yy}\frac{\partial v}{\partial y} + \xi\left[2T_{yy}\frac{\partial v}{\partial y} + T_{xy}\left(\frac{\partial u}{\partial y} + \frac{\partial v}{\partial x}\right)\right]\right) \\ &\quad + \frac{\alpha_G ReWi}{(1-\beta_n)}\left(T_{xy}^2 + T_{yy}^2\right) = 2\frac{(1-\beta_n)}{Re}\frac{\partial v}{\partial y}, \end{aligned} \tag{12}$$

$$\begin{aligned} &f(tr(\mathbf{T}))T_{xy} + Wi\left(\frac{\partial T_{xy}}{\partial t} + \frac{\partial (uT_{xy})}{\partial x} + \frac{\partial (vT_{xy})}{\partial y}\right. \\ &\quad - T_{xx}\frac{\partial v}{\partial x} - T_{xy}\frac{\partial v}{\partial y} - T_{xy}\frac{\partial u}{\partial x} - T_{yy}\frac{\partial u}{\partial y} + +\xi\left[T_{xy}\frac{\partial u}{\partial x} + \frac{1}{2}T_{yy}\right. \\ &\quad \left.\left. \times\left(\frac{\partial u}{\partial y} + \frac{\partial v}{\partial x}\right) + \frac{1}{2}T_{xx}\left(\frac{\partial u}{\partial y} + \frac{\partial v}{\partial x}\right) + T_{xy}\frac{\partial v}{\partial y}\right]\right) \\ &\quad + \frac{\alpha_G ReWi}{(1-\beta_n)}T_{xy}\left(T_{xx} + T_{yy}\right) = \frac{(1-\beta_n)}{Re}\left(\frac{\partial u}{\partial y} + \frac{\partial v}{\partial x}\right). \end{aligned} \tag{13}$$

The dimensionless Equations (9–13) model an incompressible, isothermal, and two-dimensional flow for a viscoelastic fluid using the polymer stress-tensor formulation in any flow regime. So, if:

- $\beta_n = \xi = \varepsilon = \alpha_G = 0$, the UCM model is obtained;
- $\xi = \varepsilon = \alpha_G = 0$, the Oldroyd-B model is obtained;
- $\xi = \varepsilon = 0$, and $\alpha_G > 0$, the Giesekus model is obtained;
- $\alpha_G = 0$, the PTT model is obtained.

For the conformation tensors:

$$\begin{aligned} &\frac{\partial A_{xx}}{\partial t} + \frac{\partial (uA_{xx})}{\partial x} + \frac{\partial (vA_{xx})}{\partial y} - 2A_{xx}\frac{\partial u}{\partial x} - 2A_{xy}\frac{\partial u}{\partial y} = \frac{1}{Wi} \\ &\quad \times\left[f(L) - f(\mathbf{A})A_{xx}\right] + \frac{1}{Wi}\alpha_G\left[A_{xx}(2 - A_{xx}) - A_{xy}^2 - 1\right], \end{aligned} \tag{14}$$

$$\begin{aligned} &\frac{\partial A_{yy}}{\partial t} + \frac{\partial (uA_{yy})}{\partial x} + \frac{\partial (vA_{yy})}{\partial y} - 2A_{yy}\frac{\partial v}{\partial y} - 2A_{xy}\frac{\partial v}{\partial x} = \frac{1}{Wi} \\ &\quad \times\left[f(L) - f(\mathbf{A})A_{yy}\right] + \frac{1}{Wi}\alpha_G\left[A_{yy}(2 - A_{yy}) - A_{xy}^2 - 1\right], \end{aligned} \tag{15}$$

$$\frac{\partial A_{xy}}{\partial t} + \frac{\partial (uA_{xy})}{\partial x} + \frac{\partial (vA_{xy})}{\partial y} - A_{xx}\frac{\partial v}{\partial x} - A_{yy}\frac{\partial u}{\partial y} = -\frac{1}{Wi} f(\mathbf{A})A_{xy} + \frac{1}{Wi}\alpha_G(2 - A_{xx} - A_{yy})A_{xy}. \qquad (16)$$

Note that $f(\mathbf{A}) = 1$ for the Oldroyd-B, Giesekus, and FENE-P models. So, if:

- $\beta_n = \alpha_G = 0$ and $f(L) = f(\mathbf{A}) = 1$, the UCM model is obtained;
- $\alpha_G = 0$ and $f(L) = f(\mathbf{A}) = 1$, the Oldroyd-B model is obtained;
- $f(L) = f(\mathbf{A}) = 1$, and $\alpha_G > 0$ the Giesekus model is obtained;
- $\alpha_G = 0$, $f(L) = f(\mathbf{A})$, and $f(\mathbf{A})$ defined in Equation (8), the FENE-CR model is obtained;
- $\alpha_G = 0$, $f(L) = \dfrac{L^2}{L^2 - 3}$, and $f(\mathbf{A})$ defined in Equation (7), the FENE-P model is obtained.

It would be necessary to rewrite Equation (2) in terms of the conformation tensor. However, to maintain this formulation, we will use the relations between tensors $\mathbf{A}$ and $\mathbf{T}$ (Equations 5–8) to obtain the polymer stress tensor $\mathbf{T}$.

2.1 | Polymer Stress-Tensor Calculation

The distribution of flow variables is crucial for predicting and controlling fluid behavior, and accurate prediction of flow variables is essential for designing and optimizing various engineering systems. For example, to determine the stability of the system, it acts as a reference point for analyzing disturbances and fluctuations in the flow. Additionally, flow variables distribution is necessary for the creation and verification of numerical and theoretical models that enable the prediction of flow behavior under various circumstances. We study viscoelastic plane jet flow where x and y represent the streamwise and normal directions. The laminar flow is assumed to be parallel, stationary, two-dimensional, and incompressible. The streamwise velocity of the jet flow proposed by Michalke [27] is adopted:

$$U(y) = \frac{1}{2}\left[1 + \tanh\frac{R}{4\theta}\left(\frac{R}{y} - \frac{y}{R}\right)\right], \qquad (17)$$

where θ represents the thickness of the momentum boundary layer and R the jet half-width. Given that the thickness of the shear layer has a major influence on the flow stability, the choice of laminar velocity profile based on Equation (17) allows control over the shear-layer thickness by selecting the appropriate θ. The parallel-flow approximation has been validated for jet flows through comparisons with nonparallel OpenFOAM simulations, as demonstrated in Sterza et al. [36]. This prior validation supports the applicability of the present methodology. The velocity profile is shown in Figure 1, where $R = 1$ and $\theta = 0.1$ are used in this paper. It should be emphasized that any other velocity profile can be adopted. With this profile, the technique proposed here should obtain the polymer stress-tensor components distribution.

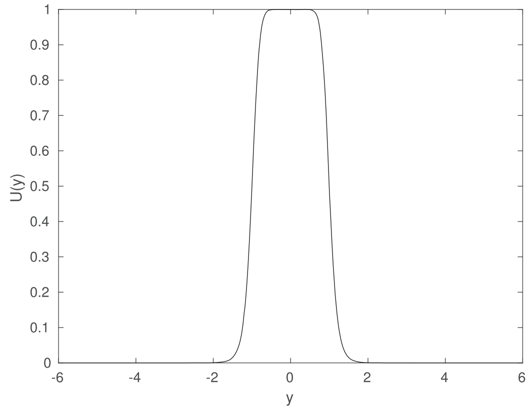

FIGURE 1 | $U(y)$ velocity profile with $R = 1$ and $\theta = 0.1$.

Fixing a velocity profile, given in Equation (17), the following assumptions are considered: parallel flow, invariance in the x direction, and $v = 0$. These assumptions are applied to Equations (11–16):

$$\frac{\partial T_{xx}}{\partial t} = -f(\mathrm{tr}(\mathbf{T}))\frac{T_{xx}}{Wi} + 2T_{xy}\frac{\partial U}{\partial y} - \xi T_{xy}\frac{\partial U}{\partial y} - \frac{\alpha_G Re}{(1-\beta_n)}\left(T_{xx}^2 + T_{xy}^2\right), \qquad (18)$$

$$\frac{\partial T_{yy}}{\partial t} = -f(\mathrm{tr}(\mathbf{T}))\frac{T_{yy}}{Wi} - \xi T_{xy}\frac{\partial U}{\partial y} - \frac{\alpha_G Re}{(1-\beta_n)}\left(T_{xy}^2 + T_{yy}^2\right), \qquad (19)$$

$$\frac{\partial T_{xy}}{\partial t} = -f(\mathrm{tr}(\mathbf{T}))\frac{T_{xy}}{Wi} + \left[T_{yy} - \frac{\xi}{2}(T_{xx} + T_{yy}) + \frac{(1-\beta_n)}{ReWi}\right] \times \frac{\partial U}{\partial y} - \frac{\alpha_G Re}{(1-\beta_n)}T_{xy}\left(T_{xx} + T_{yy}\right), \qquad (20)$$

$$\frac{\partial A_{xx}}{\partial t} = 2A_{xy}\frac{\partial U}{\partial y} + \frac{1}{Wi}\left[f(L) - f(\mathbf{A})A_{xx}\right] + \frac{1}{Wi}\alpha_G\left[A_{xx}(2 - A_{xx}) - A_{xy}^2 - 1\right], \qquad (21)$$

$$\frac{\partial A_{yy}}{\partial t} = \frac{1}{Wi}\left[f(L) - f(\mathbf{A})A_{yy}\right] + \frac{1}{Wi}\alpha_G\left[A_{yy}(2 - A_{yy}) - A_{xy}^2 - 1\right], \qquad (22)$$

$$\frac{\partial A_{xy}}{\partial t} = A_{yy}\frac{\partial U}{\partial y} - \frac{1}{Wi}f(\mathbf{A})A_{xy} + \frac{1}{Wi}\alpha_G(2 - A_{xx} - A_{yy})A_{xy}. \qquad (23)$$

These hypotheses are not considered for the Navier–Stokes equations, as the velocity profile used is fixed. The final hypothesis to be applied is that the flow is stationary. Under the Oldroyd-B model, we derive algebraic expressions for the polymer stress tensor $\mathbf{T}$ and the conformation tensor $\mathbf{A}$:

$$T_{yy} = 0, \qquad T_{xy} = \frac{(1-\beta_n)}{Re}\frac{dU}{dy}, \qquad T_{xx} = 2WiT_{xy}\frac{dU}{dy}, \qquad (24)$$

$$A_{yy} = 1, \qquad A_{xy} = Wi\frac{dU}{dy}, \qquad A_{xx} = 2WiA_{xy}\frac{dU}{dy} + 1. \qquad (25)$$

Equations (24) and (25) represent the polymer stress-tensor components and conformation-tensor components, respectively, for the Oldroyd-B model, considering the assumptions of parallel flow, invariance in the x direction, and $v = 0$. For the UCM model, just consider $\beta_n = 0$. For the other models, it is not possible to obtain an explicit expression due to the emergence of nonlinear terms between the tensors. Therefore, this article aims to find a numerical solution for the tensors in their various non-Newtonian models.

It should be noted that self-similar solutions are typically valid at sufficiently large distances downstream from the inlet, where the influence of the inlet conditions diminishes.

3 | Numerical Method

To obtain the polymer stress-tensor components for the given velocity distribution for different viscoelastic fluid models, we consider the temporal advancement of Equations (18–23). Our objective is to ensure that the temporal derivatives are zero, given that the flow is stationary, and this represents the final hypothesis we apply to these equations. We employed the fourth-order Runge–Kutta method to achieve temporal advancement (with $\Delta t = 0.1$). This process continued until reaching the established convergence restriction: $\dfrac{\max|\mathbf{T}_{\text{new}} - \mathbf{T}_{\text{old}}|}{\max|\mathbf{T}_{\text{new}}|} < 10^{-15}$, with the same restriction applied to the conformation tensor $\mathbf{A}$. As this is a jet flow, the computational domain in the y direction was stretched using mesh refinement, concentrating a large number of points at the center of the profile. 501 points were adopted in the y direction which varies from -30 to 30. Since no spatial derivative for the stress-tensor components is needed (as seen in Equations (18–23)), this number of points was adopted to provide a detailed representation of the extra-stress-tensor components. The code was implemented in OCTAVE, and each simulation lasted, on average, 3 s on a computer equipped with a 12th-generation Intel Core i7 processor and 16 GB of RAM. Generally, as the Weissenberg number increases, the simulation time also increases.

4 | Results

In this section, we present the polymer stress-tensor components for different viscoelastic models and examine the influence of their respective dimensionless parameters. All tensor components are reported in their dimensionless form, following the nondimensionalization adopted in the formulation of the governing equations. However, before delving into that, we will provide a methodological verification by comparing the results obtained with the expressions defined in Equation (24) for the Oldroyd-B and UCM models.

4.1 | Methodology Verification

To begin, we compare simulations performed using the parallel-flow approximation for the polymer stress-tensor components in the Oldroyd-B and UCM models, as given in Equation (24). We do not use the expressions in Equation (25) for this comparison because our focus is on the polymer stress tensor $\mathbf{T}$. Accordingly, when the conformation-tensor formulation is used in the code, the polymer stress is computed from $\mathbf{A}$ via the relations in Equation (5). Thus, when a figure caption indicates "Extra-Stress Tensor Code", it refers to simulations implemented directly using the extra-stress formulation given by Equations (18–20). Conversely, when the caption indicates "Conformation Tensor Code", the simulations were implemented using Equations (21–23), with the polymer stress obtained from the conformation tensor through Equation (5) for the purpose of comparison.

For notation purposes, we will use T_{xx}, T_{xy}, and T_{yy} to represent the tensors defined in Equation (24). The tensors T^E_{xx}, T^E_{xy}, and T^E_{yy} represent the values obtained from the code using the polymer stress-tensor formulation. Finally, T^A_{xx}, T^A_{xy} and T^A_{yy} represent the values obtained from the code using the conformation-tensor formulation.

Figure 2 provides a comparison between the tensors $\mathbf{T}$, $\mathbf{T}^E$, and $\mathbf{T}^A$ in the Oldroyd-B model under two sets of conditions: $Re = 100$, $\beta_n = 0.1$, and $Wi = 20$, as well as $Re = 500$, $\beta_n = 0.5$, and $Wi = 5$. On the other hand, Figure 3 compares the tensors obtained for the UCM model ($\beta_n = 0$) using $Re = 100$ and $Wi = 20$, and $Re = 500$ and $Wi = 5$. A visual analysis of these comparisons clearly shows that the results are remarkably similar. It is noticeable that the tensor T^A_{yy} seems to be distant from the others. However, upon observing the scale (10^{-18} to 10^{-19}), it becomes apparent that the results are consistent. Furthermore, it is observed that $T_{yy} = T^E_{yy} = 0$, meaning that the result obtained from the polymer stress-tensor formulation is identical for the tensors defined in Equation (24). Consequently, the results overlap in Figures 2e,f and 3e,f.

In addition to the visual analysis, we also calculated the maximum absolute error between the analytic and numerical results for each tensor component to ensure a comprehensive evaluation. This approach allows us to verify the accuracy of the results more rigorously, complementing the comparison based on visual perception. This analysis is presented in Figure 4, using the following parameters: $Re = 50$, 100, 250, 500, and 1000, $\beta_n = 0$ (UCM model), 0.25, 0.5, 0.75, and 0.9, and $Wi = 2$, 5, 10, 20, and 50. This amounts to a total of 125 cases tested, and the execution of these tests took 237 s.

Due to the variation in three parameters, we plot $\dfrac{\max|E_{\mathbf{T}}|}{\max|\mathbf{T}|}$ as a function of Wi, where $E_{\mathbf{T}} = \mathbf{T} - \mathbf{T}^X$, X is A or E, displays a wide range of results. We chose to include all results due to their ease of comprehension. Additionally, for the T_{yy} tensor, we observed that the result from the polymer stress formulation was exactly equal to the equations considering parallel-flow approximation, that is, $T_{yy} = T^E_{yy} = 0$, which explains the absence of results in Figure 4c for this formulation. An important observation is that as the Weissenberg number decreases, the absolute maximum errors also decrease.

Since the numerical method produces good results for the Oldroyd-B and UCM cases, where comparisons can be made with explicit equations for the polymer stress tensors as a function of the distribution $U(y)$, it is also justified for cases without

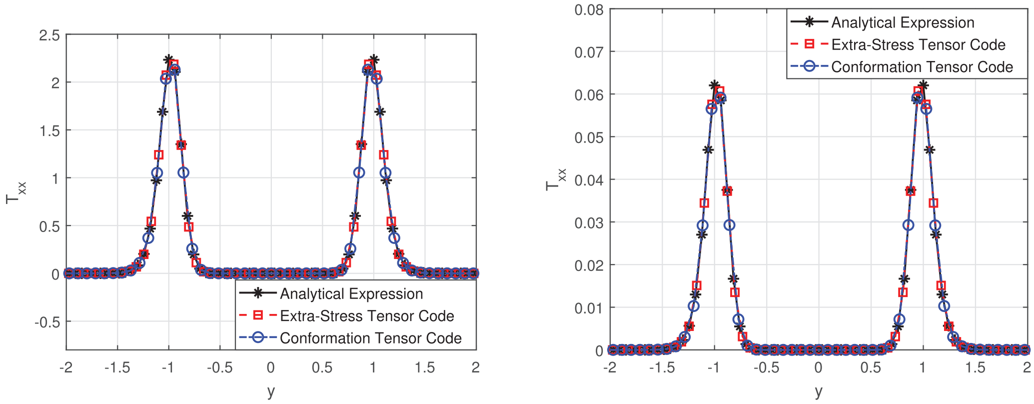

(a) T_{xx} polymer stress component.

(b) T_{xx} polymer stress component.

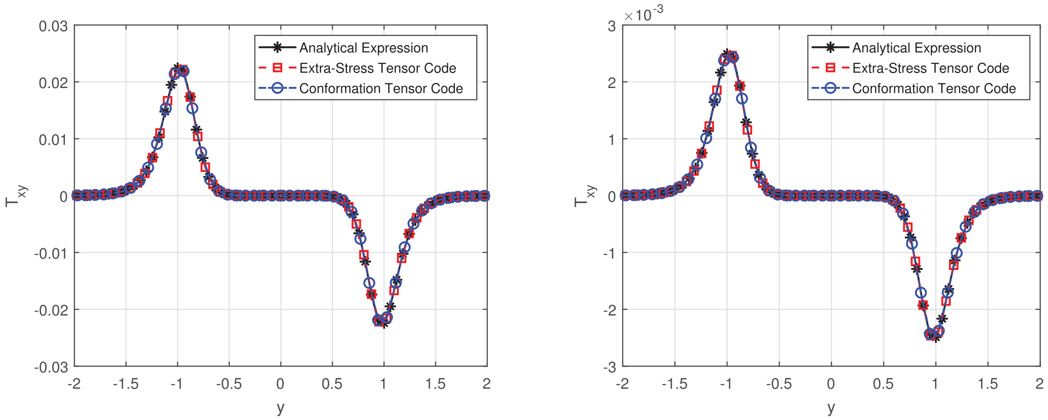

(c) T_{xy} polymer stress component.

(d) T_{xy} polymer stress component.

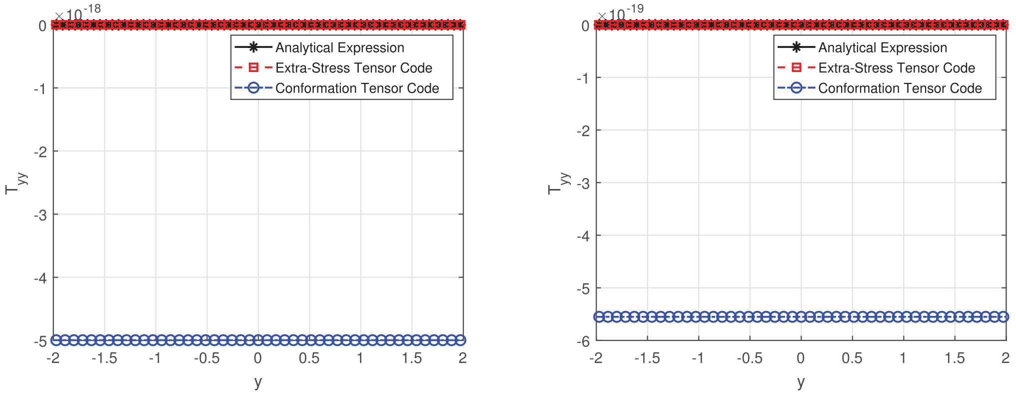

(e) T_{yy} polymer stress component.

(f) T_{yy} polymer stress component.

FIGURE 2 | Comparison of dimensionless polymer stress tensors of the Oldroyd-B model from code simulation and analytical expression (equations considering parallel-flow approximation): (left) $Re = 100$, $\beta_n = 0.1$ and $Wi = 20$; and (right) $Re = 500$, $\beta_n = 0.5$ and $Wi = 5$.

analytic equations for the stress tensors, namely, the other models presented in this paper.

Two codes were implemented, as was previously mentioned: one with the conformation-tensor formulation and the other with the polymer stress-tensor formulation. It is evident from Figures 2 and 3 that both formulations agree for the Oldroyd-B and UCM models. However, as the Giesekus model can also be obtained with both formulations, we will show its consistency in this section.

A comparison of the tensors $\mathbf{T}^E$ and $\mathbf{T}^A$ under the following two sets of parameters is given in Figure 5: $Re = 100, \beta_n = 0.1, Wi = 20$, and $\alpha_G = 0.2$; additionally, $Re = 500, \beta_n = 0.5, Wi = 5$, and $\alpha_G = 0.1$.

Once again, the visual comparison suggests good agreement between the results. However, to quantify the discrepancies, we computed the maximum absolute error between the two tensors, $\mathbf{T}^E$ and $\mathbf{T}^A$. Since no analytical solution is available for the Giesekus model, the error was normalized using $\mathbf{T}^E$ as the

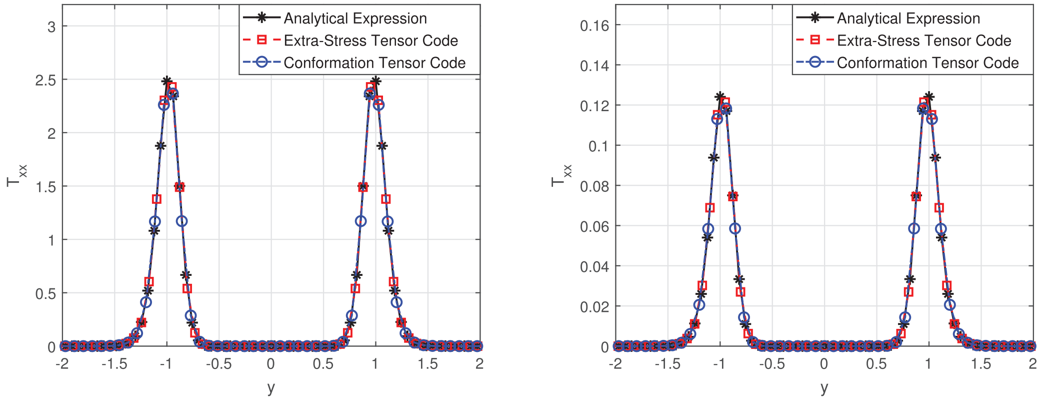

(a) T_{xx} polymer stress component.

(b) T_{xx} polymer stress component.

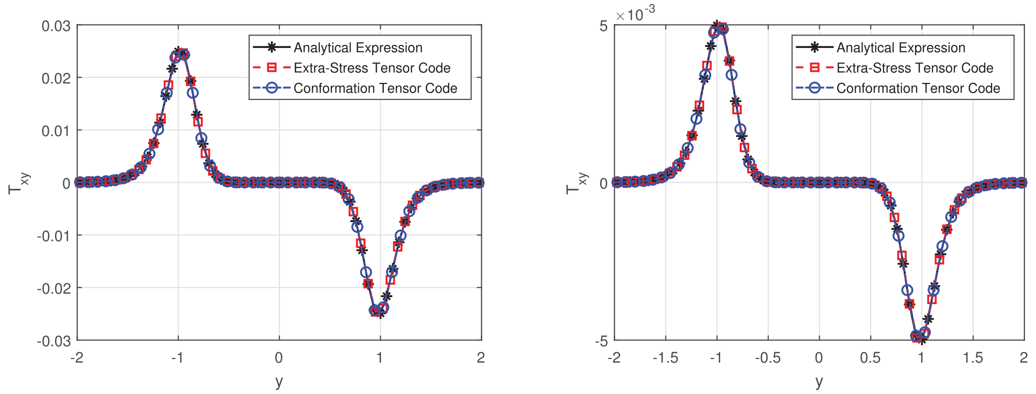

(c) T_{xy} polymer stress component.

(d) T_{xy} polymer stress component.

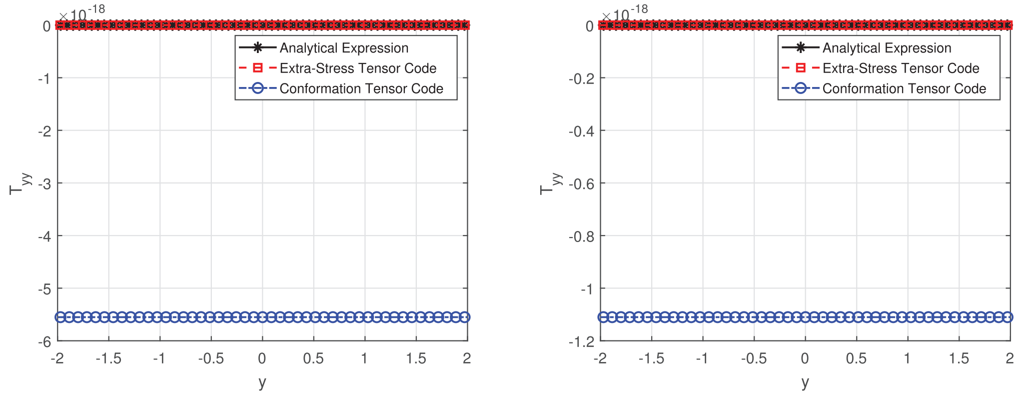

(e) T_{yy} polymer stress component.

(f) T_{yy} polymer stress component.

FIGURE 3 | Comparison of dimensionless polymer stress tensors of the UCM model ($\beta_n = 0$) from code simulation and analytical expression (equations considering parallel-flow approximation): (left) $Re = 100$ and $Wi = 20$ and (right) $Re = 500$ and $Wi = 5$.

reference, that is, by dividing the absolute difference by the maximum magnitude of $\mathbf{T}^E$. The previous set of parameters, $Re = 50$, 100, 250, 500 and 1000, $\beta_n = 0$, 0.25, 0.5, 0.75 and 0.9, and $Wi = 2$, 5, 10, 20 and 50, were used to perform the calculations, plus the mobility parameters of the Giesekus model, $\alpha_G = 0.01$, 0.1, 0.2, 0.3, 0.4 and 0.5. These results are presented in Figure 6.

The introduction of the α_G parameter, which accounts for shear-thinning behavior in the viscoelastic fluid, has a significant impact on the computed values of the stress-tensor components, as can be seen by comparing Figures 3 and 5.

The normalized errors obtained from the comparison of the two tensor fields are between 10^{-12} and 10^{-20}, demonstrating excellent consistency between the formulations. The code execution, which took 968 s to process 750 different parameter combinations, indicates that both implementations handle the parameter space consistently for this simplified scenario. These results demonstrate that the two formulations produce reliable and consistent outcomes, confirming the accuracy and robustness of the numerical implementation.

Furthermore, the parametric study covered a wide range of Weissenberg numbers ($0 < Wi < 5000$), Reynolds numbers ($0 <$

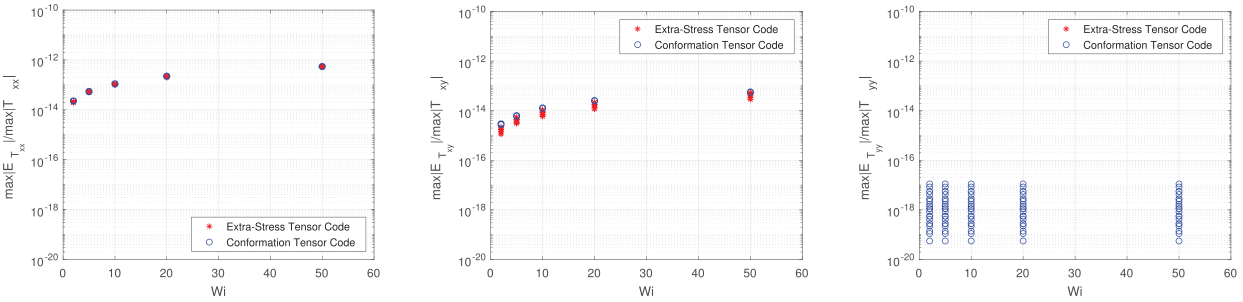

(a) max $|E_{T_{xx}}|$. (b) max $|E_{T_{xy}}|$. (c) max $|E_{T_{yy}}|$.

FIGURE 4 | Absolute maximum error, normalized by the largest magnitude of each tensor, for the Oldroyd-B and UCM models, considering $Re =$ 50, 100, 250, 500 and 1000, $\beta_n = 0$ (UCM), 0.25, 0.5, 0.75 and 0.9, and $Wi = 2, 5, 10, 20$ and 50.

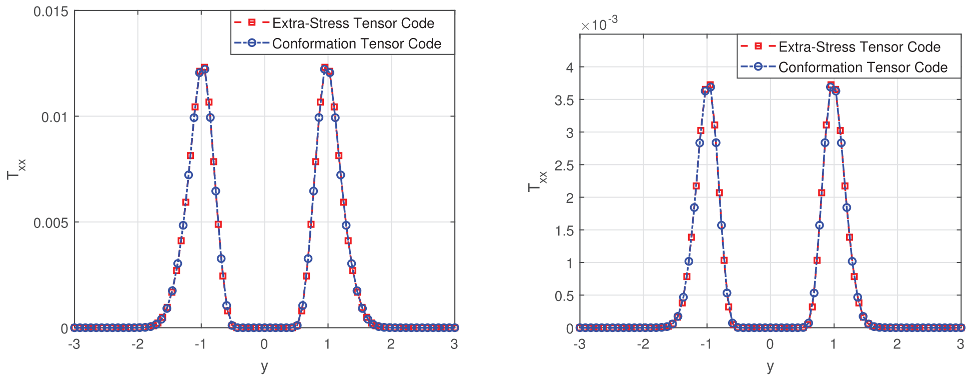

(a) T_{xx} polymer stress component. (b) T_{xy} polymer stress component.

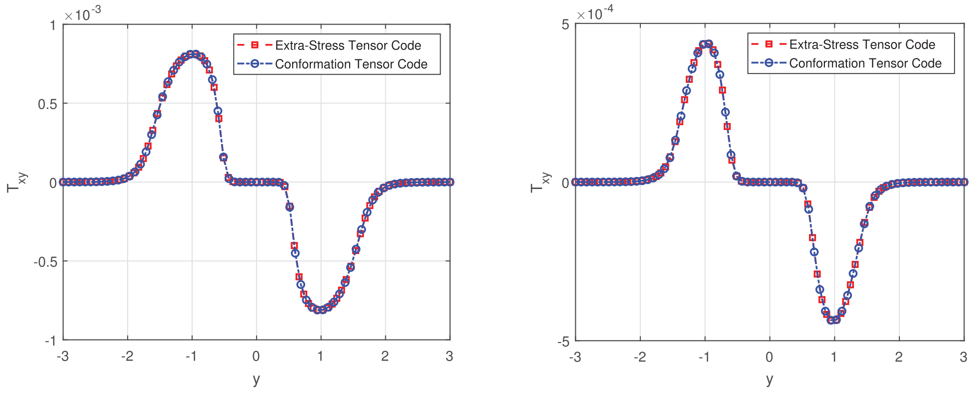

(c) T_{yy} polymer stress component. (d) T_{xx} polymer stress component.

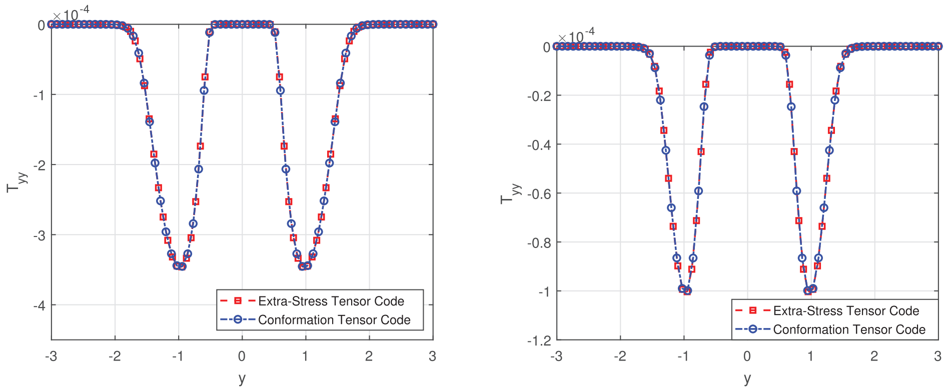

(e) T_{xy} polymer stress component. (f) T_{yy} polymer stress component.

FIGURE 5 | Comparison of dimensionless polymer stress tensors of the Giesekus model from codes simulation for the two formulations: (left) $Re = 100$, $\beta_n = 0.1$, $Wi = 20$ and $\alpha_G = 0.2$; and (right) $Re = 500$, $\beta_n = 0.5$, $Wi = 5$ and $\alpha_G = 0.1$.

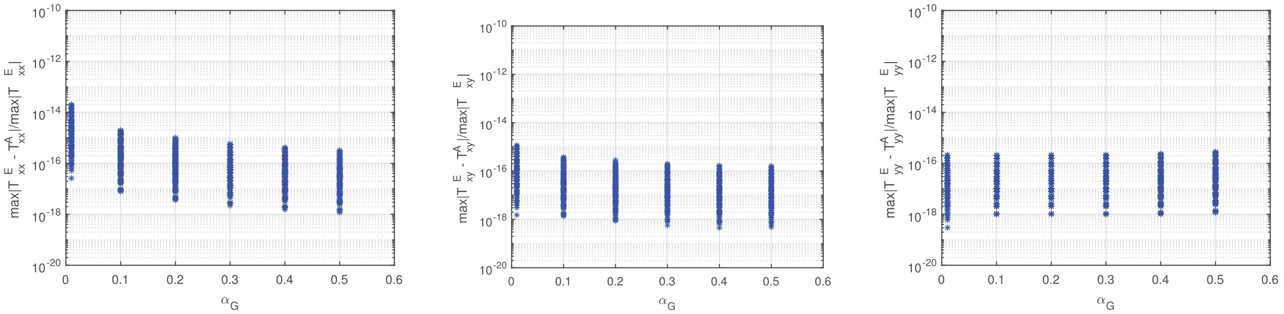

(a) $\frac{\max|\hat{T}^E_{xx} - \hat{T}^A_{xx}|}{\max|\hat{T}^E_{xx}|}$. (b) $\frac{\max|\hat{T}^E_{xy} - \hat{T}^A_{xy}|}{\max|\hat{T}^E_{xy}|}$. (c) $\frac{\max|\hat{T}^E_{yy} - \hat{T}^A_{yy}|}{\max|\hat{T}^E_{yy}|}$.

FIGURE 6 | Absolute maximum error, normalized by the largest magnitude of each tensor, between the two formulations of the Giesekus model, considering $Re = 50$, 100, 250, 500 and 1000, $\beta_n = 0$, 0.25, 0.5, 0.75 and 0.9, $Wi = 2$, 5, 10, 20 and 50, and $\alpha_G = 0.01$, 0.1, 0.2, 0.3, 0.4 and 0.5.

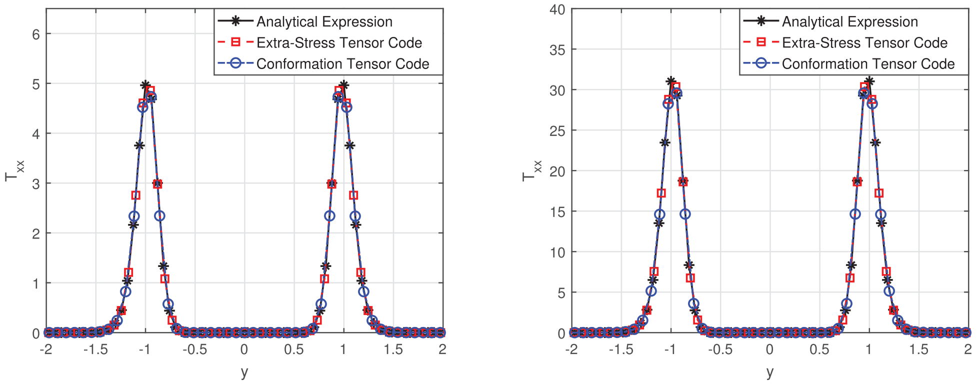

(a) T_{xx} polymer stress component. (b) T_{xy} polymer stress component.

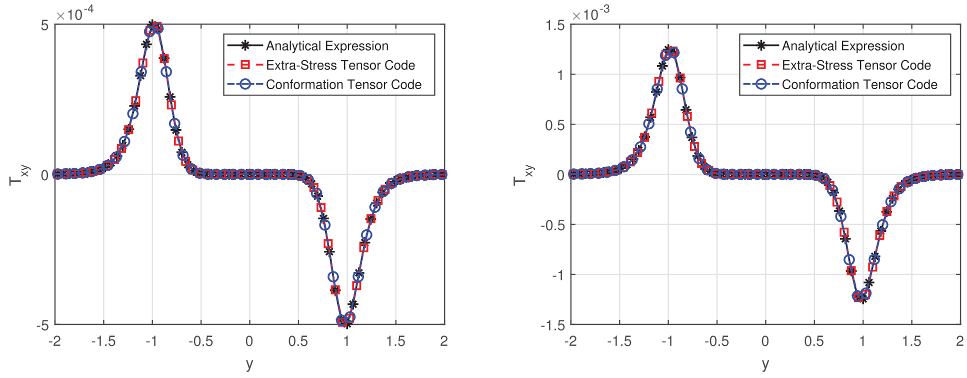

(c) T_{yy} polymer stress component. (d) T_{xx} polymer stress component.

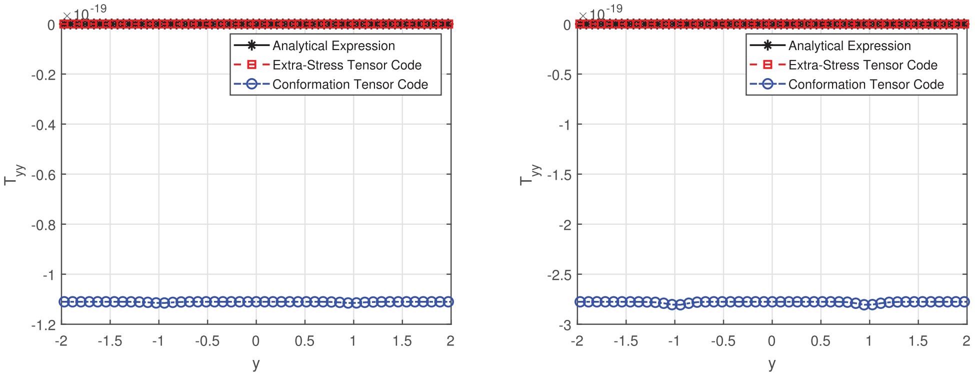

(e) T_{xy} polymer stress component. (f) T_{yy} polymer stress component.

FIGURE 7 | Comparison of dimensionless polymer stress tensors of the Oldroyd-B model from codes simulation for the two formulations: (left) $Re = 500$, $\beta_n = 0.9$ and $Wi = 2000$; and (right) $Re = 1000$, $\beta_n = 0.5$ and $Wi = 5000$.

$Re < 10,000$), and viscosity ratios ($0 \leq \beta_n < 1$). No stability limitations were observed within this interval. However, a noticeable increase in the number of iterations required for convergence was observed as Wi approached the upper end of the tested range, a behavior that will be further illustrated in the comparisons presented below.

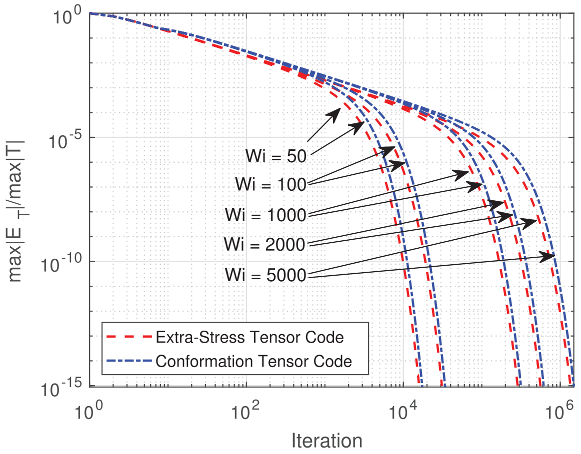

FIGURE 8 | Decay of the normalized error as a function of the iteration count for five Weissenberg numbers ($Wi = 50, 100, 1000, 2000,$ and 5000), until the prescribed convergence tolerance is reached.

Figure 7 presents a comparison among the tensors $\mathbf{T}, \mathbf{T}^E$ and $\mathbf{T}^A$ for the Oldroyd-B model under two distinct sets of conditions: $Re = 500$, $\beta_n = 0.9$, and $Wi = 2000$; and $Re = 1000$, $\beta_n = 0.5$, and $Wi = 5000$. A good agreement among the three evaluated tensors can be observed, consistent with the discussion provided above.

However, as mentioned earlier, increasing the Weissenberg number leads to a greater number of iterations (and consequently longer computational times) before convergence is achieved. This behavior is illustrated in Figure 8, which shows the decay of the normalized numerical error, $\frac{\max|E_{\mathbf{T}}|}{\max|\mathbf{T}|}$, as a function of the iteration count until the prescribed convergence tolerance is satisfied, for $Wi = 50, 100, 1000, 2000,$ and 5000, with $Re = 1000$ and $\beta_n = 0.1$.

4.2 | Giesekus Model

After analyzing the accuracy of the methodology for the Oldroyd-B, UCM, and Giesekus models, the Giesekus model is now considered for different mobility parameters.

It is observed that a decrease in the maximum amplitude for the tensor components T_{xx} and T_{xy} is a consequence of an increase in the mobility parameter α_G when comparing the results obtained in Figure 2 with those in Figure 5. On the other hand, nonzero values start to show up for the tensor component T_{yy} close to the

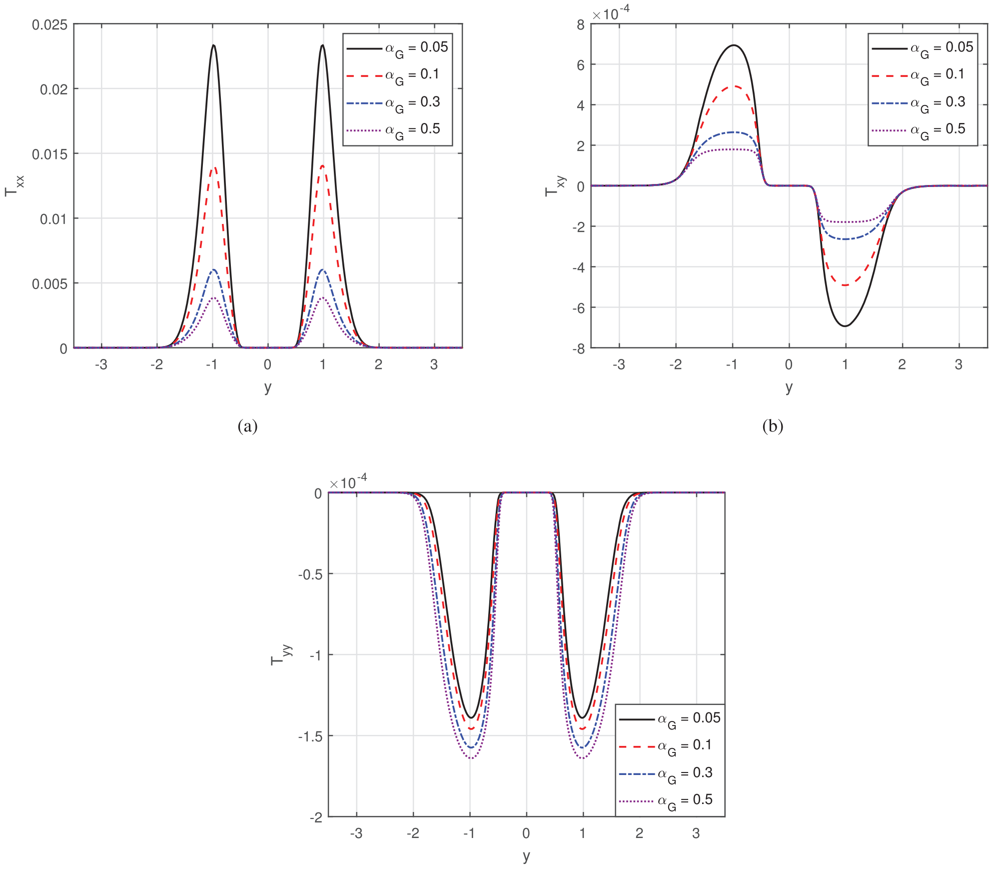

(a)

(b)

(c)

FIGURE 9 | Comparison of dimensionless polymer stress tensors obtained through simulation for the Giesekus model with different values of α_G: (a) T_{xx}, (b) T_{xy}, and (c) T_{yy} polymer stress components for $Re = 100$, $\beta_n = 0.1$, and $Wi = 50$.

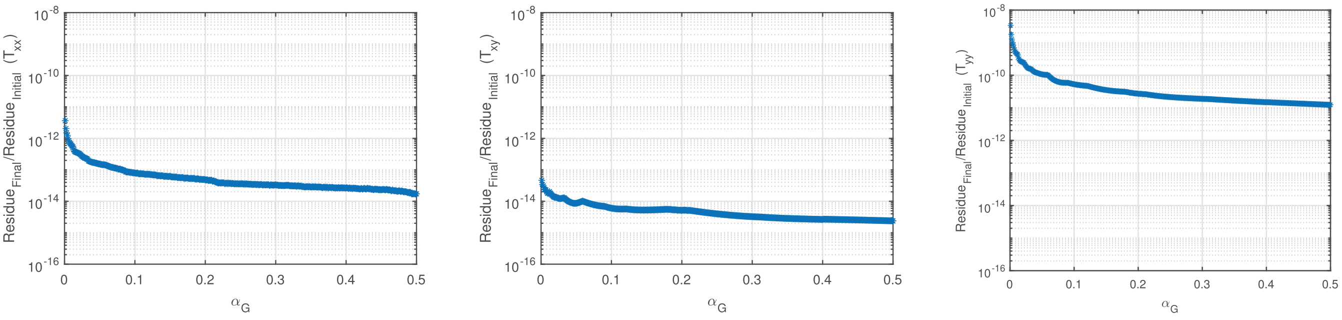

(a) (b) (c)

FIGURE 10 | Normalized residuals obtained for the Giesekus model with varying values of α_G for (a) T_{xx}, (b) T_{xy}, and (c) T_{yy} polymer stress component for $Re = 100$, $\beta_n = 0.1$, and $Wi = 50$.

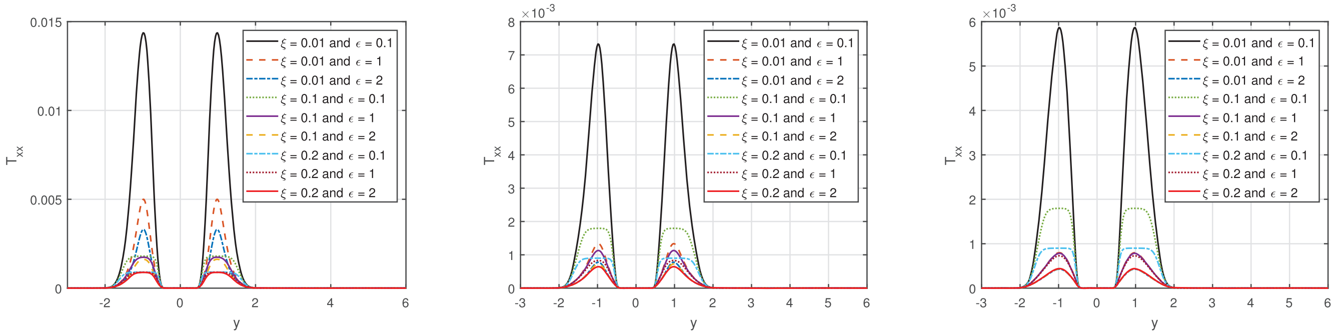

(a) T_{xx} - LPTT model. (b) T_{xx} - QPTT model. (c) T_{xx} - EPTT model.

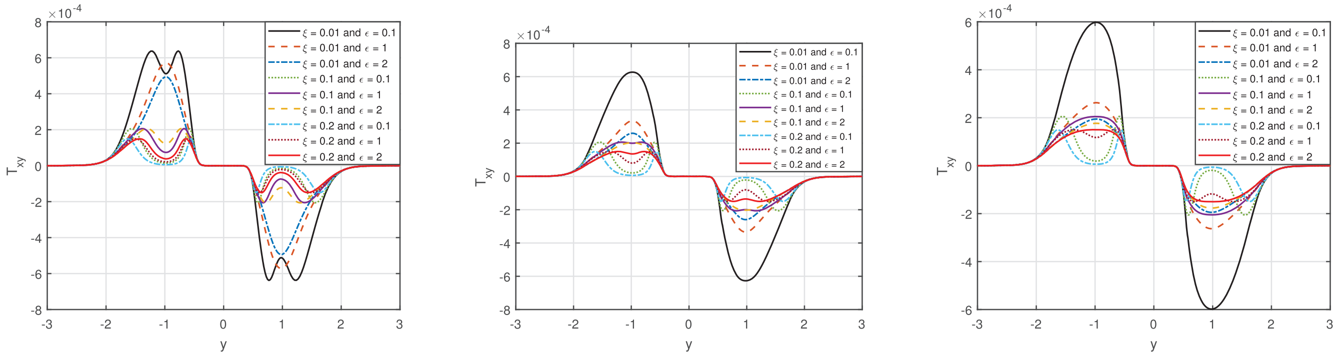

(d) T_{xy} - LPTT model. (e) T_{xy} - QPTT model. (f) T_{xy} - EPTT model.

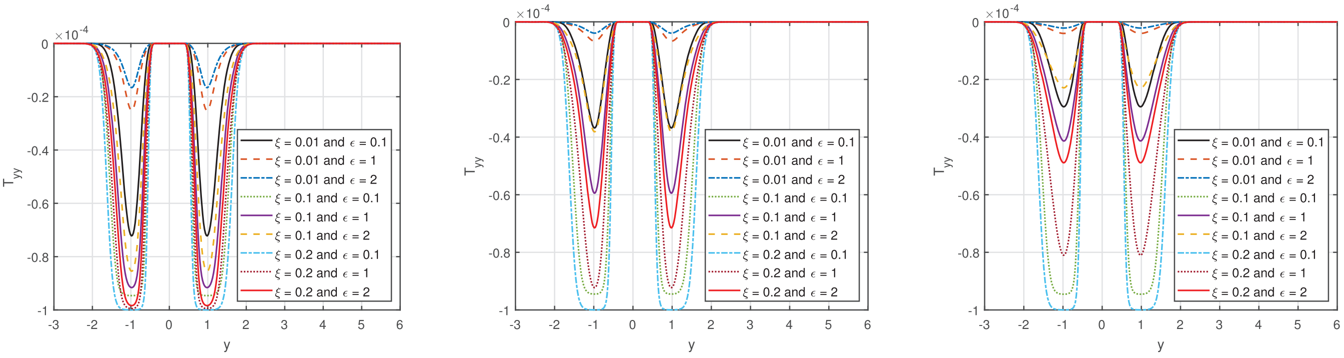

(g) T_{yy} - LPTT model. (h) T_{yy} - QPTT model. (i) T_{yy} - EPTT model.

FIGURE 11 | Comparison of dimensionless polymer stress tensors obtained through simulation for the PTT models with different values of ϵ and ξ for $Re = 100$, $\beta_n = 0.1$, and $Wi = 50$.

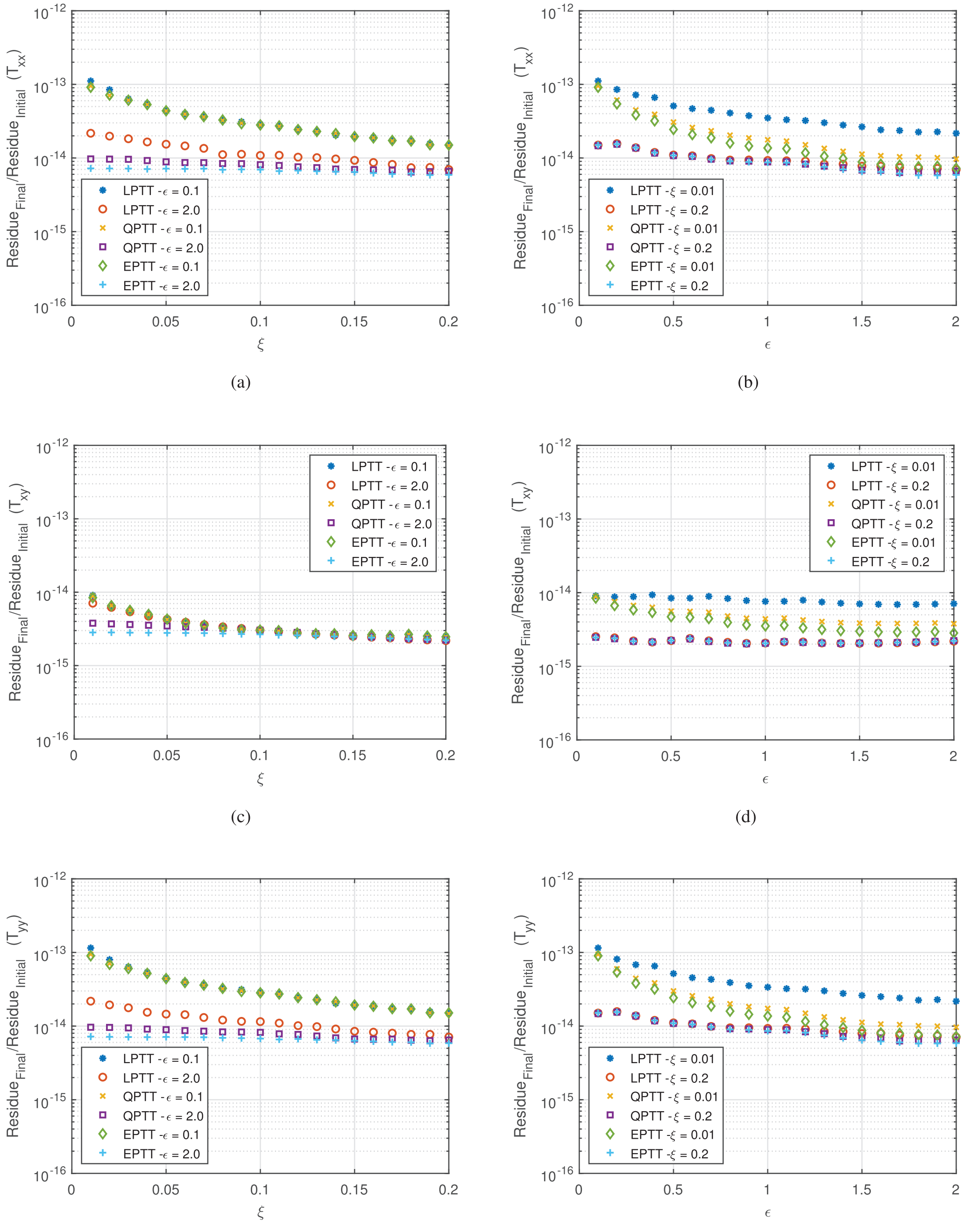

(a) (b)

(c) (d)

(e) (f)

FIGURE 12 | Normalized residuals obtained for the PTT models with varying values of ξ and ε for (a) – (b) T_{xx}, (c) – (d) T_{xy}, and (e) – (f) T_{yy} polymer stress components for $Re = 100$, $\beta_n = 0.1$, and $Wi = 50$.

jet center line region, which is consistent with the fact that the anisotropy of the fluid increases as the polymer molecules align in the flow direction.

The largest differences were found to occur at low Reynolds numbers, low values of the constant β_n, and higher Weissenberg numbers, according to the tests carried out and the data in Figure 4. For this reason, we examined how the flow behaves for different values of α_G in the following scenarios: $Re = 100$, $\beta_n = 0.1$, and $Wi = 50$. The results presented in this section were simulated using the polymer stress formulation. Tensor components T_{xx}, T_{xy}, and T_{yy} are compared for $\alpha_G = 0.05, 0.1, 0.3,$ and 0.5 in Figure 9.

It is possible to observe what was mentioned earlier: as the mobility factor α_G increases, the maximum amplitude for the components T_{xx} and T_{xy} decreases, but the amplitude of T_{yy} increases.

We computed the residual by substituting the tensor components obtained at the final iteration (i.e., after convergence of the numerical solver) into the right-hand side of Equations (18–20). Since the problem is solved under steady-state conditions, ideally,

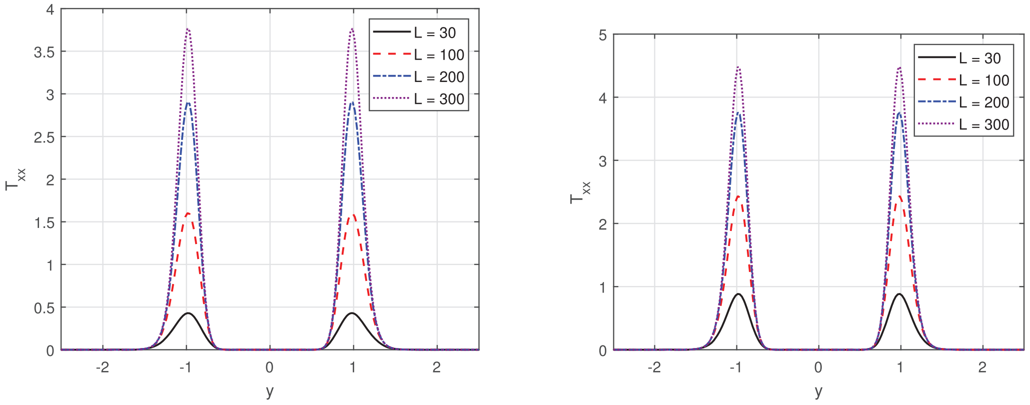

(a) T_{xx} - FENE-P model. (b) T_{xx} - FENE-CR model.

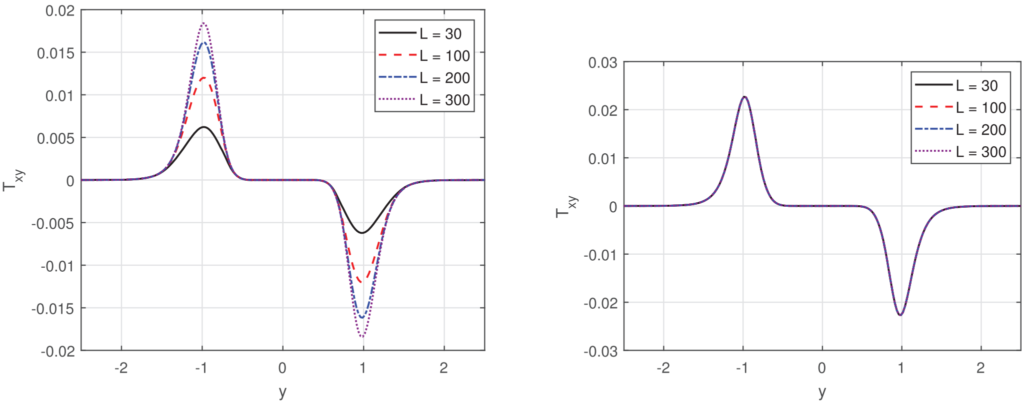

(c) T_{xy} - FENE-P model. (d) T_{xy} - FENE-CR model.

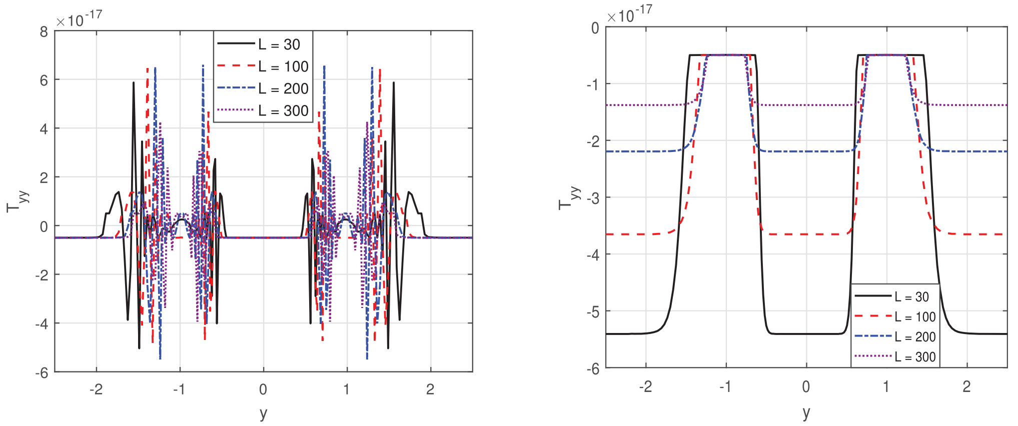

(e) T_{yy} - FENE-P model. (f) T_{yy} - FENE-CR model.

FIGURE 13 | Comparison of dimensionless polymer stress tensors obtained through simulation for the FENE models with different values of L for $Re = 100$, $\beta_n = 0.1$, and $Wi = 50$.

these expressions should be zero. To allow a consistent quantitative comparison across different values of α_G, the residual was normalized with respect to its initial value, namely $\frac{\|\mathcal{R}(\mathbf{T}^{\text{final}})\|_2}{\|\mathcal{R}(\mathbf{T}^{1})\|_2}$. The resulting normalized residuals are shown in Figure 10, using increments of 0.001 for α_G in the range $0.001 \leq \alpha_G \leq 0.5$.

It is noticeable that the residuals are close to zero (between 10^{-8} and 10^{-16}), indicating that the obtained solution can be considered stationary under the imposed assumptions.

4.3 | PTT Models

In this section, we will use the proposed model for the polymer stress-tensor components calculation and explore how they vary for different conditions, considering three PTT models: the linear (LPTT), the quadratic (QPTT), and the exponential (EPTT). The dimensionless parameters used for the simulation are the same as those used for the other models: $Re = 100$, $\beta_n = 0.1$, and $Wi = 50$. For the PTT models, additional parameters ε and ξ

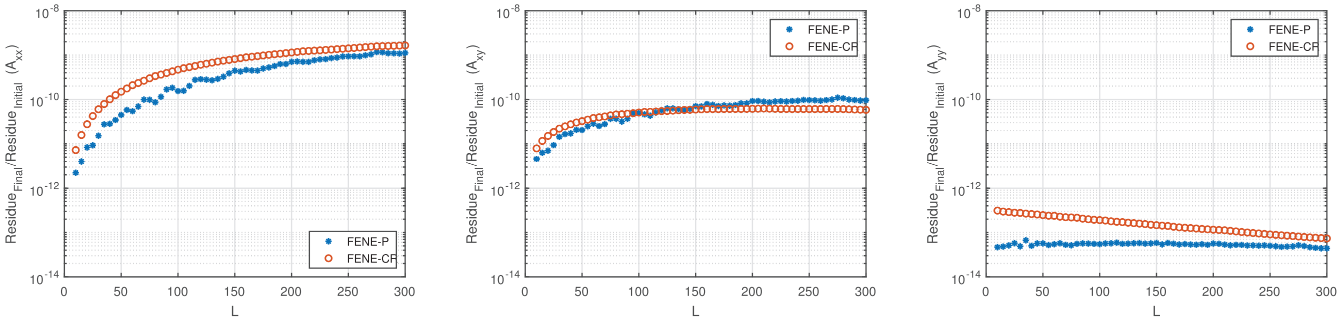

(a) (b) (c)

FIGURE 14 | Normalized residuals obtained for the FENE models with varying values of L for $Re = 100$, $\beta_n = 0.1$, and $Wi = 50$.

arise, for which the influence on the results will be evaluated through variation. The first analysis performed was to compare the tensors T_{xx}, T_{xy}, and T_{yy} for the three models using $\xi = 0.01$, 0.1, and 0.2, and $\epsilon = 0.1$, 1, and 2. These results are shown in Figure 11. It can be observed that there is a significant impact of PTT models and parameters on the observed flow patterns.

The simulations for the QPTT and EPTT models with $\Delta t = 1$ as parameter variations did not converge, so to produce these results, the time step had to be reduced to $\Delta t = 0.1$. Furthermore, as observed in the other models, it was found that the parameters ξ and ϵ have a significant impact on the maximum and minimum amplitudes of the tensor components, showing how much the differences in normal stress and anisotropy are affected by the relaxation and hardening properties of the model.

For the PTT models, the residual analysis was performed by fixing ϵ at 0.1 and 2 and varying ξ from 0.01 to 0.2 in increments of 0.1, using Equations (18–20). In addition, ϵ was varied from 0.1 to 2 in increments of 0.1 while ξ was held fixed at 0.01 and 0.2. As in the previous section, the residual corresponds to the evaluation of the converged tensor fields in the right-hand side of the constitutive equations and is reported in its normalized form (final value divided by the initial value). For all parameter combinations, the normalized residuals remain below 10^{-12} (Figure 12), confirming the robustness and consistency of the numerical procedure.

4.4 | FENE Models

The FENE-P and FENE-CR models were both tested. The results for these models came from the conformation-tensor formulation simulations. As a result, the residual is determined using Equations (21–23), and the polymer stress tensors obtained via relations (7) and (8) are compared. Comparisons the polymer stress tensors for various values of L ($L = 30, 100, 200,$ and 300), with $Re = 100$, $\beta_n = 0.1$, and $Wi = 50$, are shown in Figure 13.

The oscillations observed in Figure 13e,f are attributed to numerical round-off errors. These oscillations exhibit negligible amplitude, with values below 10^{-17}, and are effectively considered zero within the limits of numerical precision.

It is noted that the polymer extension parameter L significantly influences the polymeric tensor, showing that the normal stress component in the flow direction is the most affected component. This result shows that the model predicts correctly the effect of alignment of the polymer chain in the flow direction. Figure 14 displays the normalized residuals from the models using the same dimensionless values as previously mentioned, but with L varying in steps 5 to 300. The residuals obtained are consistent with the expected behavior for the model. It is observed that as the maximum polymer extension L increases, so does the residual for the tensor component A_{xx}. Tests with $L > 300$ were found to have residuals that likewise stay at 10^{-8}.

5 | Conclusions

This work presents a method for numerically solving the polymeric stress-tensor equations for a prescribed velocity field. The method considers the hypothesis of stationary and parallel flow (invariance in the streamwise direction and zero normal velocity component) to write simplified polymeric stress-tensor equations. The parallel assumption is applicable for boundary-layer-type flows, in the present case, for submerged jet flows.

Results are initially compared to explicit equations available for the UCM and Oldroyd-B models and then to more complex non-Newtonian models. This approach is relevant for obtaining the polymeric stress-tensor components for a given local base flow with a prescribed velocity distribution in order to perform local hydrodynamic stability analysis.

Using the proposed methodology, results are presented that show the effect of the most important non-Newtonian parameters of the different models on the resulting polymeric stress components. Increasing the mobility parameter decreases the streamwise and shear components T_{xx} and T_{xy}, but increases the absolute value of the normal tensor component T_{yy}. The effects of the elongation ϵ and anisotropy ξ parameters, controlling anisotropy, strain-hardening, and transient behavior, were observed, along with the impact of the maximum extension parameter L of the FENE models, showing a strong influence on the stress-tensor components.

Future studies will use this methodology to investigate the hydrodynamic stability of submerged non-Newtonian jets, considering both convective and absolute instability modes.

Author Contributions

Rafael de Lima Sterza: conceptualization, methodology, writing – original draft. **Leandro Franco de Souza:** methodology, supervision, writing – review and editing. **Marcio Teixeira de Mendonca:** methodology, writing – review and editing. **Analice Costacurta Brandi:** methodology, writing – review and editing. All authors have read and agreed to the published version of the manuscript.

Acknowledgments

The authors thank the *Coordenação de Aperfeiçoamento de Pessoal de Nível Superior* (CAPES) for the research grant received during the development of this study. The research was carried out using the computational resources of the Center for Mathematical Sciences Applied to Industry (CeMEAI), funded by FAPESP (grant 2013/07375-0).

Funding

This work was supported by the Coordenação de Aperfeiçoamento de Pessoal de Nível Superior and the Fundação de Amparo à Pesquisa do Estado de São Paulo (Grant No. 2013/07375-0).

Conflicts of Interest

The authors declare no conflicts of interest.

Data Availability Statement

The data that support the findings of this study are available from the corresponding author upon reasonable request.

References

1. I. Pérez-Reyes, R. O. Vargas-Aguilar, S. B. Pérez-Vega, and A. S. Ortiz-Pérez, "Applications of Viscoelastic Fluids Involving Hydrodynamic Stability and Heat Transfer," in *Polymer Rheology*, ed. J. L. Rivera-Armenta and B. A. Salazar Cruz (IntechOpen, 2018).

2. A. Beris, R. Armstrong, and R. Brown, "Spectral/Finite-Element Calculations of the Flow of a Maxwell Fluid Between Eccentric Rotating Cylinders," *Journal of Non-Newtonian Fluid Mechanics* 22 (1987): 129–167.

3. G. Mompean and M. Deville, "Unsteady Finite Volume of Oldroyd-B Fluid Through a Three-Dimensional Planar Contraction," *Journal of Non-Newtonian Fluid Mechanics* 72 (1997): 253–279.

4. E. Brasseur, M. Fyrillas, G. Georgiou, and M. Crochet, "The Time-Dependent Extrudate-Swell Problem of an Oldroyd-B Fluid With Slip Along the Wall," *Journal of Rheology* 42 (1994): 549–566.

5. T. N. Phillips and A. Williams, "Comparison of Creeping and Inertial Flow of an Oldroyd-B Fluid Through a Planar and Axisymmetric Contraction," *Journal of Non-Newtonian Fluid Mechanics* 108 (2002): 25–47.

6. F. T. Pinho, M. A. Alves, and P. J. Oliveira, "Benchmark Solutions for the Flow of Oldroyd-B and PTT Fluids in Planar Contractions," *Journal of Non-Newtonian Fluid Mechanics* 10 (2003): 45–75.

7. H. Giesekus, "A Simple Constitutive Equation for Polymer Fluids Based on the Concept of Deformation-Dependent Tensorial Mobility," *Journal of Non-Newtonian Fluid Mechanics* 11 (1982): 69–109.

8. A. I. Leonov, "Nonequilibrium Thermodynamics and Rheology of Viscoelastic Polymer Media," *Rheologica Acta* 15 (1976): 85–98.

9. R. B. Bird, P. J. Dotson, and N. L. Johnson, "Polymer Solution Rheology Based on a Finitely Extensible Bead-Spring Chain Model," *Journal of Non-Newtonian Fluid Mechanics* 7 (1980): 213–235.

10. M. D. Chilcott and J. M. Rallison, "Creeping Flow of Dilute Polymer Solutions Past Cylinders and Spheres," *Journal of Non-Newtonian Fluid Mechanics* 29 (1988): 381–432.

11. N. Phan-Thien and R. I. Tanner, "A New Constitutive Equation Derived From Network Theory," *Journal of Non-Newtonian Fluid Mechanics* 2 (1977): 353–365.

12. R. G. Larson, *Constitutive Equations for Polymer Melts and Solutions* (Butterworth-Heinemann, 1988).

13. A. Kaye, *Non-Newtonian Flow in Incompressible Fluids*. Technical Report (College of Aeronautics Cranfield, 1962).

14. X. L. Luo and R. I. Tanner, "A Streamline Element Scheme for Solving Viscoelastic Flow Problems Part II: Integral Constitutive Models," *Journal of Non-Newtonian Fluid Mechanics* 22 (1986): 61–89.

15. X. L. Luo and R. I. Tanner, "Finite Element Simulation of Long and Short Circular Die Extrusion Experiments Using Integral Models," *International Journal for Numerical Methods in Engineering* 25 (1988): 9–22.

16. J. Y. Yoo and H. C. Choi, "On the Steady Simple Shear Flows of the One-Mode Giesekus Fluid," *Rheologica Acta* 28, no. 1 (1989): 13–24.

17. G. Schleiniger and R. J. Weinacht, "Steady Poiseuille Flows for a Giesekus Fluid," *Journal of Non-Newtonian Fluid Mechanics* 40, no. 1 (1991): 79–102.

18. P. J. Oliveira, "An Exact Solution for Tube and Slit Flow of a FENE-P Fluid," *Acta Mechanica* 158, no. 3–4 (2002): 157–167.

19. T. Hayat, A. M. Siddiqui, and S. Asghar, "Some Simple Flows of an Oldroyd-B Fluid," *International Journal of Engineering Science* 39, no. 2 (2001): 135–147.

20. T. Hayat, M. Khan, and M. Ayub, "Exact Solutions of Flow Problems of an Oldroyd-B Fluid," *Applied Mathematics and Computation* 151, no. 1 (2004): 105–119.

21. A. Raisi, M. Mirzazadeh, A. S. Dehnavi, and F. Rashidi, "An Approximate Solution for the Couette–Poiseuille Flow of the Giesekus Model Between Parallel Plates," *Rheologica Acta* 47, no. 1 (2008): 75–80.

22. M. F. Tomé, M. T. Araujo, J. D. Evans, and S. McKee, "Numerical Solution of the Giesekus Model for Incompressible Free Surface Flows Without Solvent Viscosity," *Journal of Non-Newtonian Fluid Mechanics* 263 (2019): 104–119.

23. L. J. S. Furlan, M. T. Araujo, A. C. Brandi, D. O. A. Cruz, and L. F. Souza, "Different Formulations to Solve the Giesekus Model for Flow Between Two Parallel Plates," *Applied Sciences* 11, no. 21 (2021): 10115.

24. M. T. A. Araujo, L. J. S. Furlan, A. C. Brandi, and L. F. Souza, "A Semi-Analytical Method for Channel and Pipe Flows for the Linear Phan-Thien-Tanner Fluid Model With a Solvent Contribution," *Polymers* 14, no. 21 (2022): 4675.

25. H. Schlichting, *Boundary-Layer Theory*, 7th ed. (McGraw-Hill, 1979).

26. P. K. Kundu, I. M. Cohen, and D. R. Dowling, *Fluid Mechanics*, 6th ed. (Academic Press, 2015).

27. A. Michalke, *Instabilität eines kompressiblen runden Freistrahls unter Berücksichtigung des Einflusses der Strahlgrenzschichtdichte* (Deutsche Forschungs-und Versuchsanst. für Luft-und Raumfahrt, 1971).

28. G. E. Mattingly and C. C. Chang, "Unstable Waves on an Axisymmetric Jet Column," *Journal of Fluid Mechanics* 65, no. 3 (1974): 541–560.

29. A. Michalke, "Survey on Jet Instability Theory," *Progress in Aerospace Sciences* 21 (1984): 159–199.

30. P. J. Morris, "The Spatial Viscous Instability of Axisymmetric Jets," *Journal of Fluid Mechanics* 77, no. 3 (1976): 511–529.

31. P. J. Morris, "Viscous Stability of Compressible Axisymmetric Jets," *AIAA Journal* 21, no. 4 (1983): 481–482.

32. S. Parvar, C. B. Silva, and F. T. Pinho, "Local Similarity Solution for Steady Laminar Planar Jet Flow of Viscoelastic FENE-P Fluids," *Journal of Non-Newtonian Fluid Mechanics* 279 (2020): 104265.

33. M. C. Guimarães, N. Pimentel, F. T. Pinho, and C. B. Silva, "Direct Numerical Simulations of Turbulent Viscoelastic Jets," *Journal of Fluid Mechanics* 899 (2020): A11.

34. M. C. Guimarães, F. T. Pinho, and C. B. Silva, "Viscoelastic Jet Instabilities Studied by Direct Numerical Simulations," *Physical Review Fluids* 8 (2023): 103301.

35. R. L. Sterza, L. F. Souza, M. T. Mendonca, and A. C. Brandi, "Shooting and Matrix Method Applied to the Analysis of Stability of Viscoelastic Jet Flows," in *Proceedings of the 13th Spring School on Transition and Turbulence*, *Blumenau, Brazil* (2022).

36. R. L. Sterza, M. T. Mendonca, L. F. de Souza, and A. C. Brandi, "Investigation of the Stability of a Planar Oldroyd-B Jet," *Journal of the Brazilian Society of Mechanical Sciences and Engineering* 45 (2023): 251.

37. R. L. Sterza, L. F. Souza, A. Cavalieri, M. T. Mendonca, and A. C. Brandi, "Stability Analysis of Oldroyd-B and Giesekus Fluids in a Planar Jet Flow," in *Proceedings of the 27th International Congress of Mechanical Engineering*, *Florianópolis, Brazil* (2023).

38. S. Yamani, Y. Raj, T. A. Zaki, G. H. McKinley, and I. Bischofberger, "Spatiotemporal Signatures of Elastoinertial Turbulence in Viscoelastic Planar Jets," *Physical Review Fluids* 8 (2023): 064610.

39. M. D. Torres, B. Hallmark, D. I. Wilson, and L. Hilliou, "Natural Giesekus Fluids: Shear and Extensional Behavior of Food Gum Solutions in the Semidilute Regime," *AICHE Journal* 60, no. 11 (2014): 3902–3915.

40. N. Phan-Thien, "A Nonlinear Network Viscoelastic Model," *Journal of Rheology* 22, no. 3 (1978): 259–283.

41. F. T. Pinho and P. J. Oliveira, "Axial Annular Flow of a Nonlinear Viscoelastic Fluid — An Analytical Solution," *Journal of Non-Newtonian Fluid Mechanics* 93, no. 2 (2000): 325–337.